

FUTON: Fourier Tensor Network for Implicit Neural Representations

Pooya Ashtari*
 Ghent University
 pooya.ashtari@ugent.be

Nikos Deligiannis
 Vrije Universiteit Brussel (VUB)
 ndeligia@etrovub.be

Pourya Behmandpoor
 Vrije Universiteit Brussel (VUB)
 pourya.behmandpoor@vub.be

Aleksandra Pižurica
 Ghent University
 aleksandra.pizurica@ugent.be

Abstract

*Implicit neural representations (INRs) have emerged as powerful tools for encoding signals, yet dominant MLP-based designs often suffer from slow convergence, overfitting to noise, and poor extrapolation. We introduce **FUTON (Fourier Tensor Network)**, which models signals as generalized Fourier series whose coefficients are parameterized by a low-rank tensor decomposition. FUTON implicitly expresses signals as weighted combinations of orthonormal, separable basis functions, combining complementary inductive biases: Fourier bases capture smoothness and periodicity, while the low-rank parameterization enforces low-dimensional spectral structure. We provide theoretical guarantees through a universal approximation theorem and derive an inference algorithm with complexity linear in the spectral resolution and the input dimension. On image and volume representation, FUTON consistently outperforms state-of-the-art MLP-based INRs while training 2–5× faster. On inverse problems such as image denoising and super-resolution, FUTON generalizes better and converges faster.*

1. Introduction

Implicit Neural Representations (INRs), also known as *neural fields*, have emerged as a powerful paradigm for representing signals, including images, volumes, and radiance fields. Unlike grid-based representations that store signals as discrete arrays (*e.g.*, pixels or voxels), INRs encode signals as continuous functions parameterized by neural network weights, mapping coordinates to signal values. This coordinate-based parameterization offers key advantages: (1) *resolution independence*, enabling super-resolution without retraining; (2) *memory efficiency* through compact parameter storage; (3) natural handling of *irregular sampling*; and

(4) *differentiability* with respect to coordinates, facilitating gradient-based optimization for inverse problems.

INRs have demonstrated strong performance across diverse tasks, including 3D reconstruction [6, 13], view synthesis [12], and inverse problems [19, 27]. Typical INRs employ multilayer perceptrons (MLPs) with specialized activations, *e.g.*, periodic sine functions [20], Gaussian nonlinearities [17], or complex Gabor wavelets [18], all of which significantly outperform ReLU-based networks for signal representation [16].

MLP-based INRs suffer from three key limitations: (1) *slow convergence*, leading to long training times; (2) susceptibility to *overfitting*, when regularization is insufficient; and (3) *poor generalization* to unobserved regions, critical for inverse problems. These issues arise because MLPs lack inductive biases aligned with the low-dimensional structure of natural signals.

We introduce *Fourier Tensor Network* (**FUTON**), a novel INR that addresses these challenges by expressing signals as *generalized Fourier series* whose coefficients are parameterized via a *low-rank tensor decomposition*. This design embeds complementary inductive biases: Fourier bases capture smoothness and periodicity, while low-rank factorization captures the intrinsic low-dimensional spectral structure of natural signals. Unlike MLP-based INRs that learn arbitrary nonlinear mappings, FUTON’s shallow architecture inherently favors smooth, structured representations, yielding faster convergence and improved generalization.

FUTON leverages the insight that structured signals exhibit frequency-domain correlations amenable to low-rank approximation. With a Canonical Polyadic (CP) decomposition [11], FUTON achieves linear complexity via efficient tensor contractions and is supported by a *universal approximation theorem*.

We validate FUTON’s effectiveness across diverse applications in signal representation and inverse problems. For signal representation, FUTON substantially outperforms

*Corresponding author

state-of-the-art MLP-based INRs such as WIRE [18] while converging significantly faster. FUTON also demonstrates strong generalization on challenging inverse problems, including image super-resolution and CT reconstruction.

Contributions. Our main contributions are:

- **Novel architecture:** We propose FUTON, combining generalized Fourier series with a low-rank tensor decomposition, providing an alternative to MLP-based INRs.
- **Theoretical foundations:** We prove a universal approximation theorem establishing that FUTON can represent any L^2 function to arbitrary precision.
- **Computational efficiency:** We establish FUTON’s linear complexity through efficient tensor contraction, enabling scalability to high-dimensional signals.
- **Superior performance:** Extensive experiments demonstrate that FUTON achieves higher reconstruction quality, faster convergence, and better generalization on inverse problems compared to state-of-the-art methods.

Notation. Vectors are denoted by bold lowercase (*e.g.*, \mathbf{x}), matrices by bold uppercase (*e.g.*, \mathbf{U}), tensors by calligraphic bold uppercase (*e.g.*, \mathcal{W}), and sets by blackboard bold uppercase (*e.g.*, \mathbb{X}). Individual elements are indexed by subscripts in non-bold notation: $x_i, U_{ij}, \mathcal{W}_{ijk}$. Non-negative integers are denoted by \mathbb{N}_0 .

2. Related Work

Implicit Neural Representations. NeRF [12] popularized representing scenes as continuous radiance fields parameterized by MLPs, enabling high-quality novel view synthesis. Subsequent work extended INRs to dynamic scenes [14, 15], shape representation [6, 13], and generative modeling [3], establishing INRs as a fundamental tool in visual computing.

MLP-based INRs. Most INRs adopt MLP backbones whose inductive bias is strongly shaped by the activation function and input encoding. ReLU MLPs exhibit a low-frequency bias and struggle to fit fine detail [16]. Fourier features mitigate this by mapping coordinates to high-dimensional sinusoidal embeddings [23]. SIREN employs sinusoidal activations with principled initialization for stable optimization [20]. Alternatives include Gaussian activations [17] and complex Gabor wavelets (WIRE) [18], which improve space-frequency localization. Nevertheless, training large MLPs can be slow and hyperparameter-sensitive, and parameter counts scale poorly with resolution.

Tensor Networks. Tensor decompositions and tensor networks provide compact models for multi-dimensional data [11]. Canonical Polyadic (CP) [2, 7] expresses a tensor as a sum of rank-1 components, while Tucker [24] introduces

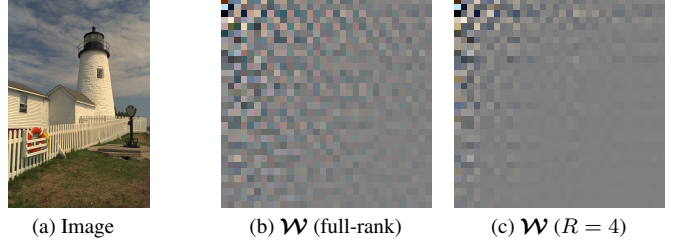


Figure 1. **FUTON weight tensor visualization.** (a) Original image from the Kodak dataset ($C = 2, D = 3$). The FUTON model uses $K = 32$ cosine basis functions per dimension, yielding a weight tensor $\mathcal{W} \in \mathbb{R}^{32 \times 32 \times 3}$. Visualizations of \mathcal{W} as RGB images for (b) full-rank and (c) low-rank ($R = 4$). The low-rank representation captures the dominant spectral structure.

a low-rank core with factor matrices. In the INR context, TensoRF [4] factorizes radiance fields into low-rank components; K-Planes [5] extends factorization to dynamic scenes; and F-INR [25] decomposes high-dimensional tasks into lightweight MLP sub-networks. Unlike these methods that factorize spatial domains or architectures, FUTON uniquely factorizes *Fourier coefficients*, combining frequency-domain analysis with tensor networks for computational efficiency.

Frequency-Domain Representations. Frequency-domain ideas are used to counter the spectral bias of coordinate MLPs. Fourier positional encodings [23] and periodic activations [18, 20] inject high frequencies directly into the representation. More recently, the Fourier reparameterization method learns coefficient matrix of fixed Fourier bases to compose the weights of MLPs. Unlike these approaches that modulate inputs, nonlinearities, or weights, FUTON *eliminates the MLP entirely* by directly parameterizing the Fourier coefficients of the signal via a low-rank tensor decomposition.

Inverse Problems. INRs have been applied to inverse problems such as super-resolution [26] and medical image reconstruction [19, 27]. NeRP [19] learns frequency-selective positional encodings, NAF [27] introduces neural attenuation fields for CT, and COIL [22] combines coordinate-based optimization with implicit regularization across imaging tasks. These methods often rely on task-specific architectures or explicit regularizers to avoid overfitting measurement noise. By contrast, FUTON’s low-rank spectral parameterization acts as an intrinsic prior, enabling data-efficient reconstructions with minimal task-specific tuning.

3. Preliminaries

3.1. Implicit Neural Representation

INRs are functions $f_\theta : \mathbb{R}^C \rightarrow \mathbb{R}^D$ parameterized by neural networks with learnable parameters θ that map contin-

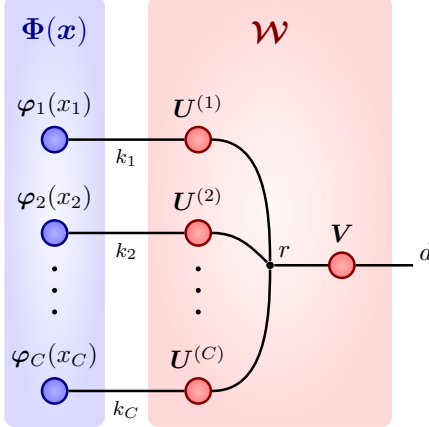


Figure 2. Tensor diagram of FUTON’s forward pass. Nodes represent tensors, connected edges represent contracted indices (summed over), and dangling edges correspond to open indices. Refer to Section 8.1 in the supplementary materials for tensor diagram notation.

uous coordinates to signal values. For instance, in image representation, $\mathbf{x} = (x_1, x_2)$ represents pixel coordinates, and $\mathbf{f}_\theta(\mathbf{x}) \in \mathbb{R}^3$ outputs RGB values. Given a ground-truth signal $\mathbf{s}(\mathbf{x})$, the goal is to learn parameters θ such that $\mathbf{s}(\mathbf{x}) \approx \mathbf{f}_\theta(\mathbf{x})$. This is typically achieved by minimizing the mean squared error over observed coordinate-signal pairs $\{(\mathbf{x}_n, \mathbf{s}_n)\}_{n=1}^N$, where $\mathbf{s}_n = \mathbf{s}(\mathbf{x}_n)$.

Typical INRs use MLPs with layer output $\mathbf{y}^{(\ell)} = \sigma(\mathbf{W}^{(\ell)} \mathbf{y}^{(\ell-1)} + \mathbf{b}^{(\ell)})$, where σ is the activation function, $\mathbf{W}^{(\ell)}, \mathbf{b}^{(\ell)}$ are weights and biases, $\mathbf{y}^{(0)} = \mathbf{x} \in \mathbb{R}^C$ is the input, and $\mathbf{y}^{(L+1)} = \mathbf{W}^{(L+1)} \mathbf{y}^{(L)} + \mathbf{b}^{(L+1)}$ is the output. Activation choice critically affects capacity. Leading activations include periodic $\sigma(\mathbf{x}) = \sin(\omega_0 \mathbf{x})$ (SIREN [20]), Gaussian $\sigma(\mathbf{x}) = e^{-(s_0 \mathbf{x})^2}$ [17], and complex Gabor $\sigma(\mathbf{x}) = e^{j\omega_0 \mathbf{x}} e^{-|s_0 \mathbf{x}|^2}$ (WIRE [18]).

3.2. Generalized Fourier Series

Fourier series decomposes signals into trigonometric components, enabling compact representation through frequency selectivity. The *Generalized Fourier series (GFS)* [] extends this idea to arbitrary orthonormal bases and higher-dimensional spaces, offering flexibility for representing diverse signal classes.

Orthogonal Basis. A set of functions $\{\varphi_k\}_{k \in \mathbb{N}_0} \subseteq L^2(\mathbb{X})$ (refer to Section 7 in supplementary materials for definition) is an **orthonormal basis (ONB)** for $L^2(\mathbb{X})$ if it satisfies the following properties:

- (i) **Orthonormality:** $\langle \varphi_k, \varphi_\ell \rangle_{L^2} = \delta_{k\ell}$ for all $k, \ell \in \mathbb{N}_0$, where $\delta_{k\ell}$ is the Kronecker delta; and
- (ii) **Completeness:** For any function $f \in L^2(\mathbb{X})$, there exist coefficients $w_k \in \mathbb{R}$ for $k \in \mathbb{N}_0$ such that the partial sums $s_K = \sum_{k=0}^{K-1} w_k \varphi_k$ converge to f in $L^2(\mathbb{X})$ as $K \rightarrow \infty$.

See Definition 9 in supplementary materials for a formal definition of ONB. In other words, an ONB is a set of orthonormal functions that can approximate any function in $L^2(\mathbb{X})$ arbitrarily well by a finite linear combination of functions from that set. As a canonical example, the cosine functions

$$\varphi_0(x) = 1, \quad \varphi_k(x) = \sqrt{2} \cos(k\pi x) \quad (k \geq 1) \quad (1)$$

form an ONB in $L^2([0, 1])$, widely studied in Fourier analysis [21].

Separable Multi-dimensional Basis. Let $\{\varphi_k\}_{k \in \mathbb{N}_0}$ be a set of one-dimensional functions in $L^2([0, 1])$. We construct a set of *separable* multi-dimensional functions in $L^2([0, 1]^C)$ by products of the one-dimensional basis functions:

$$\phi_{\mathbf{k}}(\mathbf{x}) \triangleq \prod_{c=1}^C \varphi_{k_c}(x_c), \quad (2)$$

where $\mathbf{k} = (k_1, \dots, k_C) \in \mathbb{N}_0^C$ are multi-indices, and $\mathbf{x} = (x_1, \dots, x_C) \in [0, 1]^C$ are coordinates.

Theorem 1 (Separable Basis Orthonormality). *If $\{\varphi_k\}_{k \in \mathbb{N}_0}$ is an ONB for $L^2([0, 1])$, then $\{\phi_{\mathbf{k}}\}_{\mathbf{k} \in \mathbb{N}_0^C}$ defined in (2) forms an ONB for $L^2([0, 1]^C)$.*

Proof. See Section 9 in supplementary materials. \square

Generalized Fourier Series. For a vector-valued function $\mathbf{s}(\mathbf{x}) = [s_1(\mathbf{x}), \dots, s_d(\mathbf{x})]^\top$ with $s_d \in L^2([0, 1]^C)$ for $d \in \{1, \dots, D\}$, the partial sum of *generalized Fourier series (GFS)* [] using the ONB $\{\phi_{\mathbf{k}}\}_{\mathbf{k} \in \mathbb{K}}$ (defined in (2)) is defined by

$$\hat{s}_K(\mathbf{x}) \triangleq \sum_{\mathbf{k} \in \mathbb{K}} \mathbf{w}^{(\mathbf{k})} \phi_{\mathbf{k}}(\mathbf{x}), \quad (3)$$

where $\mathbb{K} = \{0, \dots, K-1\}^C$ is a finite truncation of all multi-indices, and the coefficient vector $\mathbf{w}^{(\mathbf{k})} = [w_1^{(\mathbf{k})}, \dots, w_D^{(\mathbf{k})}]^\top \in \mathbb{R}^D$ has components obtained via inner products:

$$w_d^{(\mathbf{k})} = \langle s_d, \phi_{\mathbf{k}} \rangle_{L^2} = \int_{[0, 1]^C} s_d(\mathbf{x}) \phi_{\mathbf{k}}(\mathbf{x}) d\mathbf{x}. \quad (4)$$

Theorem 2 (GFS Convergence). *The partial sum \hat{s}_K converges to \mathbf{s} in $L^2([0, 1]^C)$, i.e., $\|s_d - \hat{s}_{d,K}\|_{L^2} \rightarrow 0$ as $K \rightarrow \infty$ for all $d \in \{1, \dots, D\}$.*

Proof. See Section 10 in supplementary materials. \square

Definition 1 (Generalized Dot Product). *For tensors $\mathbf{A} \in \mathbb{R}^{I_1 \times \dots \times I_M}$ and $\mathbf{B} \in \mathbb{R}^{I_1 \times \dots \times I_M \times J_1 \times \dots \times J_P}$, the generalized dot product $\mathbf{C} = \mathbf{A} \bullet \mathbf{B} \in \mathbb{R}^{J_1 \times \dots \times J_P}$ contracts over all M dimensions of \mathbf{A} :*

$$c_{j_1, \dots, j_P} = \sum_{i_1=1}^{I_1} \dots \sum_{i_M=1}^{I_M} a_{i_1, \dots, i_M} b_{i_1, \dots, i_M, j_1, \dots, j_P}. \quad (5)$$

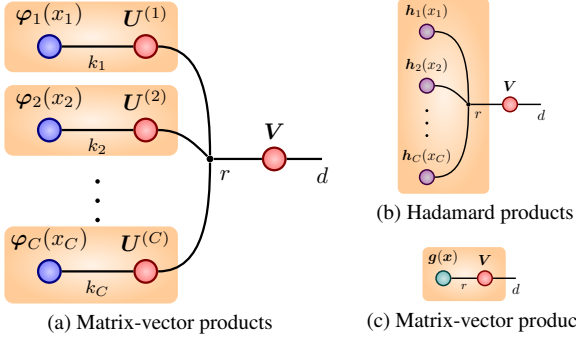


Figure 3. Optimal contraction order in FUTON’s forward pass. The computation has linear complexity $\mathcal{O}(CKR + CR + DR)$, proceeding in three stages, where yellow boxes indicate the tensors being contracted at each step: (a) project each basis vector $\varphi_c(x_c)$ onto its factor matrix $\mathbf{U}^{(c)}$ via matrix-vector multiplication (11), incurring $\mathcal{O}(CKR)$ operations; (b) combine the projected features $\mathbf{h}_c(x_c)$ via Hadamard product (10), incurring $\mathcal{O}(CR)$ operations; and (c) map the resulting vector $\mathbf{g}(\mathbf{x})$ to the output via matrix-vector multiplication with \mathbf{V} (9), incurring $\mathcal{O}(DR)$ operations. This contrasts with the naive approach of directly computing $\Phi(\mathbf{x}) \bullet \mathbf{W}$, which requires $\mathcal{O}(K^C D)$ operations and scales exponentially with the input dimension C .

Tensor Representation. The multi-dimensional basis functions in (2) can be expressed as elements of the tensor product (see Section 8.2 in supplementary materials for definition of tensor product):

$$\Phi(\mathbf{x}) = \varphi(x_1) \otimes \varphi(x_2) \otimes \cdots \otimes \varphi(x_C), \quad (6)$$

where $\Phi(\mathbf{x}) \in \mathbb{R}^{K \times \cdots \times K}$ is a *rank-1 Cth-order tensor*, and $\varphi(\mathbf{x}) = [\varphi_0(\mathbf{x}), \dots, \varphi_{K-1}(\mathbf{x})]^\top$ with $\{\varphi_k\}_{k \in \mathbb{N}_0}$ being the one-dimensional basis from (1).

Now let $\mathbf{W} = [w_d^{(\mathbf{k})}] \in \mathbb{R}^{K \times \cdots \times K \times D}$ denote the weight tensor of order $C + 1$, where $w_d^{(\mathbf{k})}$ is the coefficient for basis function $\phi_{\mathbf{k}}$ and output dimension d , as defined in (4). Using the generalized dot product from Definition 1, the GFS in (3) can be compactly expressed as

$$\hat{s}_K(\mathbf{x}) = \Phi(\mathbf{x}) \bullet \mathbf{W}. \quad (7)$$

To illustrate, consider an image with $C = 2$ and $D = 3$ (RGB) from the Kodak dataset (Figure 1a). Using $K = 32$ cosine basis functions (1) for each spatial dimension yields a feature tensor $\Phi(\mathbf{x}) \in \mathbb{R}^{32 \times 32}$ and a weight tensor $\mathbf{W} \in \mathbb{R}^{32 \times 32 \times 3}$, revealing the spectral structure visualized in Figure 1b.

4. Methods

4.1. Fourier Tensor Network (FUTON)

While the GFS provides a theoretically sound foundation, its computational complexity poses a challenge. The tensor contraction in (7) requires $\mathcal{O}(K^C D)$ operations, scaling

exponentially with input dimension C . For image representation ($C = 2, D = 3$), this requires $\mathcal{O}(3K^2)$ operations, growing quadratically with K .

To address this computational bottleneck, we *reparameterize* the weight tensor \mathbf{W} using *low-rank tensor decomposition*, yielding our *Fourier Tensor Network* (FUTON) model. Specifically, we employ the Canonical Polyadic (CP) decomposition format [11], which represents \mathbf{W} as a sum of R rank-1 tensors:

$$\mathbf{W} = \sum_{r=1}^R \mathbf{u}_r^{(1)} \otimes \mathbf{u}_r^{(2)} \otimes \cdots \otimes \mathbf{u}_r^{(C)} \otimes \mathbf{v}_r, \quad (8)$$

where $\mathbf{u}_r^{(c)} \in \mathbb{R}^K$, $\mathbf{v}_r \in \mathbb{R}^D$, and R is the CP rank. We define factor matrices $\mathbf{U}^{(c)} = [\mathbf{u}_1^{(c)} \mid \mathbf{u}_2^{(c)} \mid \cdots \mid \mathbf{u}_R^{(c)}] \in \mathbb{R}^{K \times R}$ for each input dimension c , and $\mathbf{V} = [\mathbf{v}_1 \mid \mathbf{v}_2 \mid \cdots \mid \mathbf{v}_R] \in \mathbb{R}^{D \times R}$ for the output.

In the image representation example ($C = 2, D = 3, K = 32$) shown in Figure 1, CP decomposition represents $\mathbf{W} \in \mathbb{R}^{32 \times 32 \times 3}$ with rank $R = 4$. As illustrated in Figure 1c, this low-rank factorization captures the dominant spectral structure while reducing parameters from $32 \times 32 \times 3 = 3,072$ to $2 \times 32 \times 4 + 3 \times 4 = 268$, achieving 11-fold compression. This highlights the inherent low-rank structure of natural signals in the Fourier domain, which FUTON exploits for efficient and compact representation.

Figure 2 illustrates FUTON’s tensor diagram (see Section 8.1 in supplementary materials on tensor diagram notation). Substituting (6) and (8) into (7), and subsequently rearranging the summations, yields the following compact form:

$$\mathbf{s}^{\text{futon}}(\mathbf{x}) = \mathbf{V} \mathbf{g}(\mathbf{x}), \quad (9)$$

$$\mathbf{g}(\mathbf{x}) \triangleq \mathbf{h}_1(x_1) \odot \mathbf{h}_2(x_2) \odot \cdots \odot \mathbf{h}_C(x_C), \quad (10)$$

$$\mathbf{h}_c(x_c) \triangleq \mathbf{U}^{(c)\top} \varphi(x_c), \quad c \in \{1, \dots, C\} \quad (11)$$

where $\mathbf{h}_c(x_c) \in \mathbb{R}^R$ projects basis functions at x_c onto $\mathbf{U}^{(c)}$, and $\mathbf{g}(\mathbf{x}) \in \mathbb{R}^R$ is the Hadamard product of projected features. Refer to Figure 3 for an illustrative proof using tensor diagram notation. This formulation reveals that FUTON computes weighted combinations of multiplicatively separable features.

Given observed coordinate-signal pairs $\{(\mathbf{x}_n, \mathbf{s}_n)\}_{n=1}^N$, the FUTON parameters $\theta = (\mathbf{U}^{(1)}, \dots, \mathbf{U}^{(C)}, \mathbf{V})$ are learned by minimizing the reconstruction loss:

$$\theta^* = \arg \min_{\theta} \frac{1}{N} \sum_{n=1}^N \mathcal{L}(\mathbf{s}_n, \mathbf{s}^{\text{futon}}(\mathbf{x}_n; \theta)), \quad (12)$$

where \mathcal{L} is a loss function, e.g., mean squared error. Factor matrices are initialized from a uniform distribution and optimized via gradient-based methods (e.g., Adam [9]).

Table 1. Image representation results on the Kodak dataset. The best results are **bold**, and the second-best are underlined.

Model	# Params	PSNR (dB) \uparrow	SSIM (%) \uparrow	Speed (img/s) \uparrow
ReLU+PE	542K	26.41	68.89	17.23
SIREN	528K	26.27	69.88	<u>13.07</u>
Gauss	528K	27.73	75.68	8.67
WIRE	595K	<u>33.69</u>	<u>92.38</u>	6.62
FUTON (ours)	526K	37.12	96.54	12.29

The universal approximation capacity of FUTON is established by Theorem 3. This theorem shows that FUTON can approximate any vector-valued function in $L^2([0, 1]^C)$ to arbitrary precision by choosing sufficiently large basis resolution K and rank R .

Theorem 3 (Universal Approximation). *For any $\varepsilon > 0$ and vector-valued function $\mathbf{s} \in L^2([0, 1]^C)$, there exist $K \in \mathbb{N}_0$, rank $R \leq K^{C-1} \min\{K, D\}$, and factor matrices $(\mathbf{U}^{(c)})_{c=1}^C, \mathbf{V}$ such that $\|\mathbf{s}_d - \mathbf{s}_d^{\text{futon}}\|_{L^2} < \varepsilon$ for all $d \in \{1, \dots, D\}$.*

Proof. See Section 11 in supplementary materials. \square

4.2. Computational Complexity

A key advantage of FUTON is its linear time complexity with respect to the input and output dimensions. Figure 3 illustrates the optimal contraction order (see Section 8.3 in supplementary materials). The forward pass proceeds in three stages: First, each basis vector $\varphi_c(x_c)$ is projected onto factor matrix $\mathbf{U}^{(c)}$ via matrix-vector multiplication (11), requiring $\mathcal{O}(CKR)$ operations. Second, projected features are combined through Hadamard products (10), requiring $\mathcal{O}(CR)$ operations. Third, the feature vector $\mathbf{g}(\mathbf{x})$ is mapped to the output via multiplication with \mathbf{V} (9), requiring $\mathcal{O}(DR)$ operations. Therefore, the total complexity is $\mathcal{O}(CKR + CR + DR)$, which scales linearly with the input and output dimensions C and D . The parameter count is $CKR + DR$, compared to $K^C D$ for the full tensor. Although the sufficient rank for universal approximation (Theorem 3) is bounded by $R \leq K^{C-1} \min\{K, D\}$, jeopardizing the linearity with respect to C , our ablations (Section 13) show that $R = K$ suffices for high-quality reconstruction. In PyTorch, we implement the contraction via `torch.einsum` with the `opt_einsum` backend for automatic contraction planning.

To illustrate the computational advantage, consider image representation ($C = 2, D = 3$). The original full-rank Fourier series requires $\mathcal{O}(3K^2)$ operations, while FUTON requires $\mathcal{O}(2K^2 + 5K)$ operations with $R = K$, offering substantial computational savings.

5. Experiments

We evaluate FUTON on signal representation (Section 5.2) and inverse problems (Section 5.3). All experiments are

Table 2. Occupancy volume representation results on Thai Statue data. The best results are **bold**, and the second-best are underlined.

Model	# Params	IoU (%) \uparrow	Speed (img/s) \uparrow
ReLU+PE	226k	97.51	0.30
SIREN	207k	96.71	<u>0.23</u>
Gauss	207k	97.60	0.15
WIRE	204k	<u>99.08</u>	0.12
FUTON (ours)	197k	99.67	0.19

implemented in PyTorch and run on a single NVIDIA RTX 4060 GPU (16 GB).

5.1. Experimental Setup

Baselines. We compare FUTON to four MLP-based INRs: (1) *ReLU+PE* [12] with sinusoidal positional encodings; (2) *SIREN* [20] with periodic sine activations ($\omega_0 = 20$); (3) *Gauss* [17] with Gaussian nonlinearities ($s_0 = 10$); and (4) *WIRE* [18] with complex Gabor wavelets ($\omega_0 = 20, s_0 = 10$).

Model Configurations. Input coordinates are normalized to $[-1, 1]$ for baselines and $[0, 1]$ for FUTON to enable the use of the cosine basis in (1). Signal values are normalized to $[-1, 1]$, and a $\tanh(\cdot)$ activation is applied at the output layer of all models to enforce this range. For FUTON, we set the rank to $R = K$ to reduce the hyperparameter space. All models are matched in capacity (approximately 500K parameters for 2D and 200K for 3D) to ensure a fair comparison.

Training Details. All models are optimized using the Adam optimizer [9]. Learning rates are selected for each method for optimal convergence via grid search over $\{10^{-4}, 10^{-3}, 10^{-2}, 10^{-1}\}$. We use a cosine-annealing schedule that decays the learning rate by $10 \times$ over training. Models are trained for 2000 epochs with a batch size of 10% of all coordinates. Unless otherwise specified, the loss function \mathcal{L} in (12) is the mean squared error, $\mathcal{L}(\mathbf{s}, \hat{\mathbf{s}}) = \|\mathbf{s} - \hat{\mathbf{s}}\|^2$.

Evaluation Metrics. For 2D images, we assess reconstruction quality using Peak Signal-to-Noise Ratio (PSNR) in dB and Structural Similarity Index (SSIM) in percentage. For 3D occupancy volumes, we report Intersection over Union (IoU) in percentage. Inference efficiency is measured in images per second (img/s).

5.2. Signal Representation

We first evaluate FUTON’s ability to represent continuous signals directly from coordinate-value pairs. This assesses

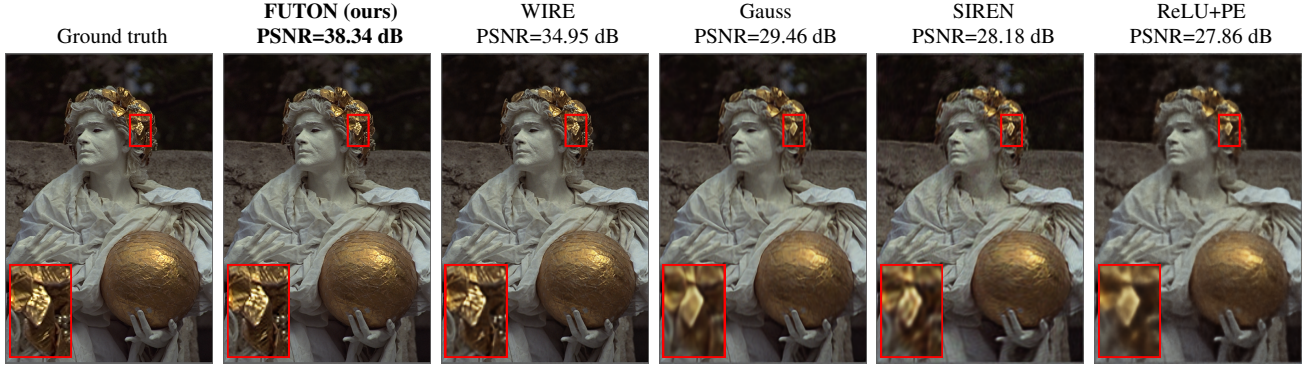


Figure 4. **Comparison on image representation.** FUTON produces sharper reconstructions with better detail preservation than baselines. The image (kodim17) is from the Kodak dataset.

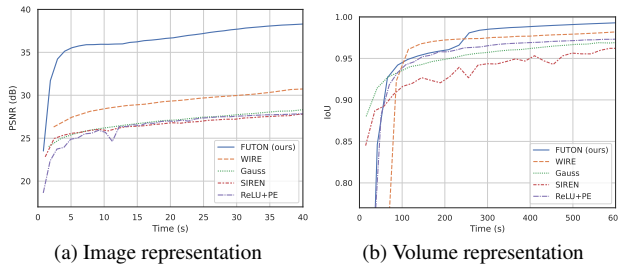


Figure 5. **Learning speed on signal representation.** PSNR and IoU versus training time for image (kodim17) and occupancy volume (Thai Statue) representation tasks.

representational capacity and convergence without the confounds of inverse problems.

5.2.1. Images

We evaluate on the Kodak dataset [10], containing 24 high-quality natural images. Table 1 reports results averaged over all images. FUTON (with $R = K = 512$) achieves 37.12 dB PSNR and 96.54% SSIM, outperforming all baselines. Compared to the strongest baseline WIRE (33.69 dB, 92.38%), FUTON improves PSNR by +3.43 dB and SSIM by +4.16 percentage points.

Figure 5a shows the convergence behavior on a representative image. FUTON converges faster than all baselines, reaching high PSNR within the first few seconds. This rapid convergence stems from FUTON’s factorized representation capturing the low-rank spectral structure inherent in natural images. While ReLU+PE achieves the highest inference speed (17.23 img/s), it produces the lowest quality. FUTON balances both, achieving 12.29 img/s (nearly twice as fast as WIRE) with substantially higher quality.

Qualitative comparisons (Figure 4) reveal that FUTON produces sharper reconstructions with better-preserved fine details and textures. Periodic activation methods (SIREN, WIRE) exhibit artifacts, while FUTON remains cleaner and more faithful to the ground truth.

5.2.2. Occupancy Volumes

We evaluate 3D signals using the Thai Statue model from the Stanford 3D Scanning Repository. Unlike continuous-valued images, occupancy volumes are binary functions indicating whether a point lies inside ($s = 1$) or outside ($s = 0$) the object, presenting a challenging 3D binary classification task.

The results are reported in Table 2. FUTON (with $R = K = 256$) achieves 99.67% IoU, outperforming the second-best method WIRE (99.08%) by 0.59 percentage points. Moreover, as shown in Figure 5b, FUTON converges faster than WIRE and Gauss, reaching high IoU in less wall-clock time.

Figure 6 provides qualitative comparisons. FUTON produces the smoothest surface reconstruction, closely matching the ground truth. Baselines exhibit artifacts: WIRE and Gauss show surface irregularities, while SIREN and ReLU+PE produce geometric distortions. These results demonstrate FUTON’s effectiveness in representing both continuous-valued (images) and discrete-valued (occupancy) signals across different dimensionalities.

5.3. Inverse Problems

We evaluate FUTON on inverse problems that recover signals from incomplete or corrupted measurements. These tasks demand implicit regularization and generalization beyond observed data, which can be challenging for INRs.

5.3.1. Image Super-Resolution

We recover high-resolution images from $4 \times$ downsampled observations. We select a representative image from the DIV2K dataset [1], train on the downsampled version, and evaluate at the original resolution. We include bilinear interpolation as a classical non-learning baseline.

Figure 7 presents visual comparisons. FUTON (with $R = K = 384$) achieves 30.74 dB PSNR, outperforming WIRE (30.54 dB) and substantially exceeding Gauss (28.52 dB), SIREN (25.23 dB), and ReLU+PE (24.97 dB).

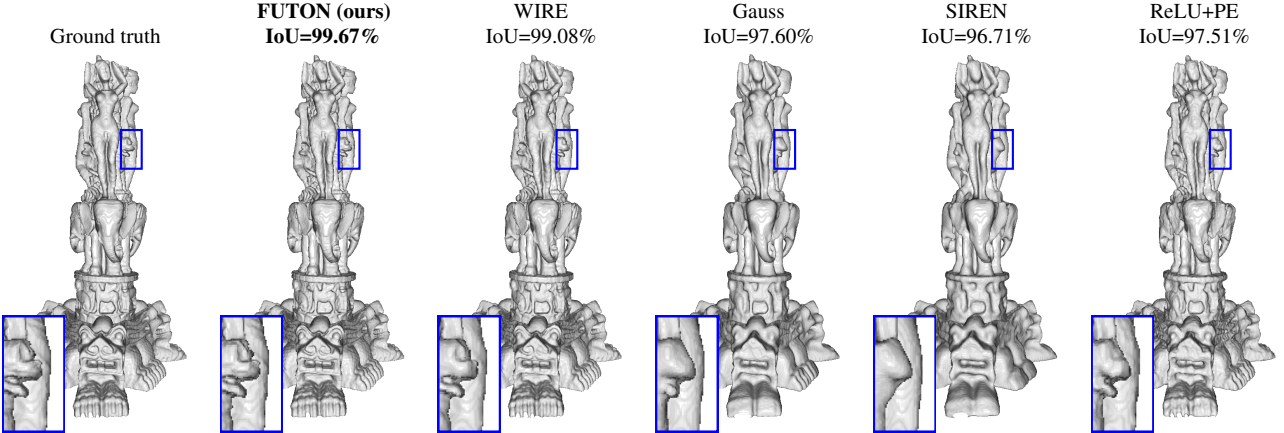


Figure 6. **Comparison on occupancy volume representation.** FUTON achieves the highest fidelity reconstruction of the Thai Statue occupancy volume, with smoother surfaces and fewer artifacts compared to baseline methods.

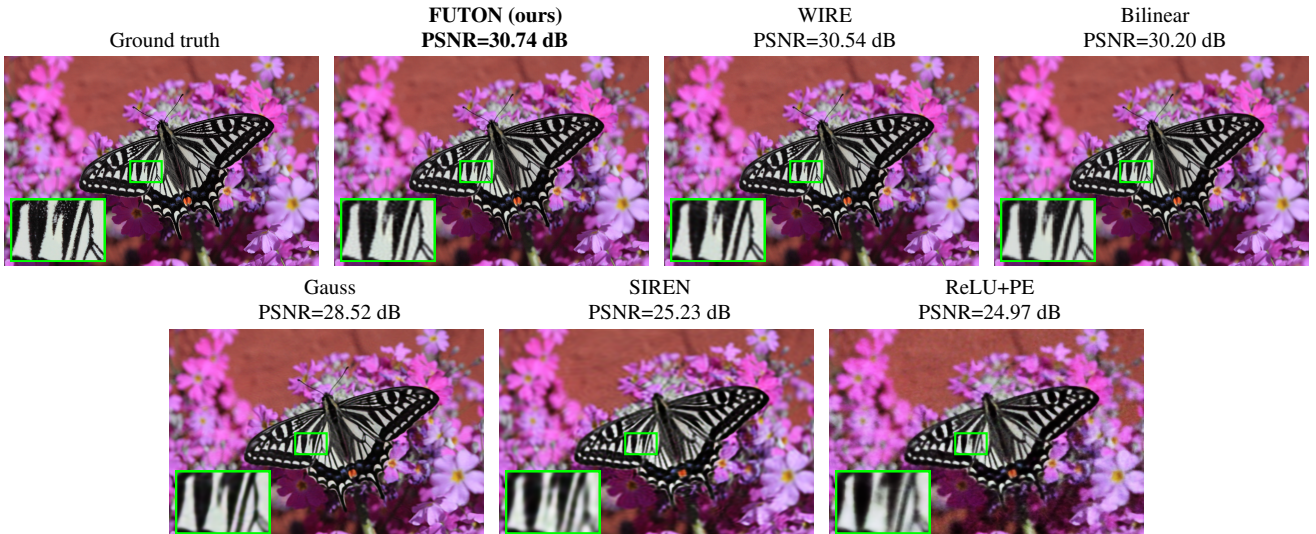


Figure 7. **Comparison on 4× image super-resolution.** FUTON recovers high-frequency details more accurately than baselines, producing sharper reconstructions that exceed even bilinear interpolation. The image is taken from the DIV2K dataset.

It also improves upon bilinear interpolation by 0.54 dB, which directly exploits the downsampling operator. This suggests stronger generalization, with implicit regularization that favors smooth, natural-looking images without explicitly incorporating priors about the downsampling process.

Qualitatively, FUTON produces sharper edges and better-preserved details. WIRE shows comparable quality with slight texture blurring. Some baselines (*e.g.*, SIREN, ReLU+PE) generate overly smooth reconstructions lacking detail, highlighting FUTON’s effectiveness for tasks requiring generalization beyond observed measurements.

5.3.2. Image Denoising

We denoise a DIV2K image downsized to $510 \times 411 \times 3$, corrupted with a sensor noise model combining photon noise

(mean count $\tau = 50$) and readout noise (standard deviation $\sigma = 1$), yielding a 20.57 dB noisy observation. To mitigate overfitting to noise, we augment the loss with total variation (TV) regularization for FUTON and all baselines: $\mathcal{L}_{\text{total}} = \mathcal{L}_{\text{MSE}} + \lambda \mathcal{L}_{\text{TV}}$ ($\lambda = 1 \times 10^{-7}$), encouraging piecewise-smooth reconstructions while preserving edges.

Figure 8 provides visual comparisons. FUTON (with $R = K = 256$) achieves the highest denoised PSNR of 27.04 dB, a 6.47 dB improvement over the noisy input and 0.53 dB above WIRE. FUTON produces cleaner reconstructions in homogeneous regions with less residual noise. Gauss (24.18 dB) introduces blurring, while SIREN (21.07 dB) and ReLU+PE (21.70 dB) retain substantial artifacts. FUTON’s low-rank factorization provides effective implicit regularization, capturing low-dimensional structure while rejecting

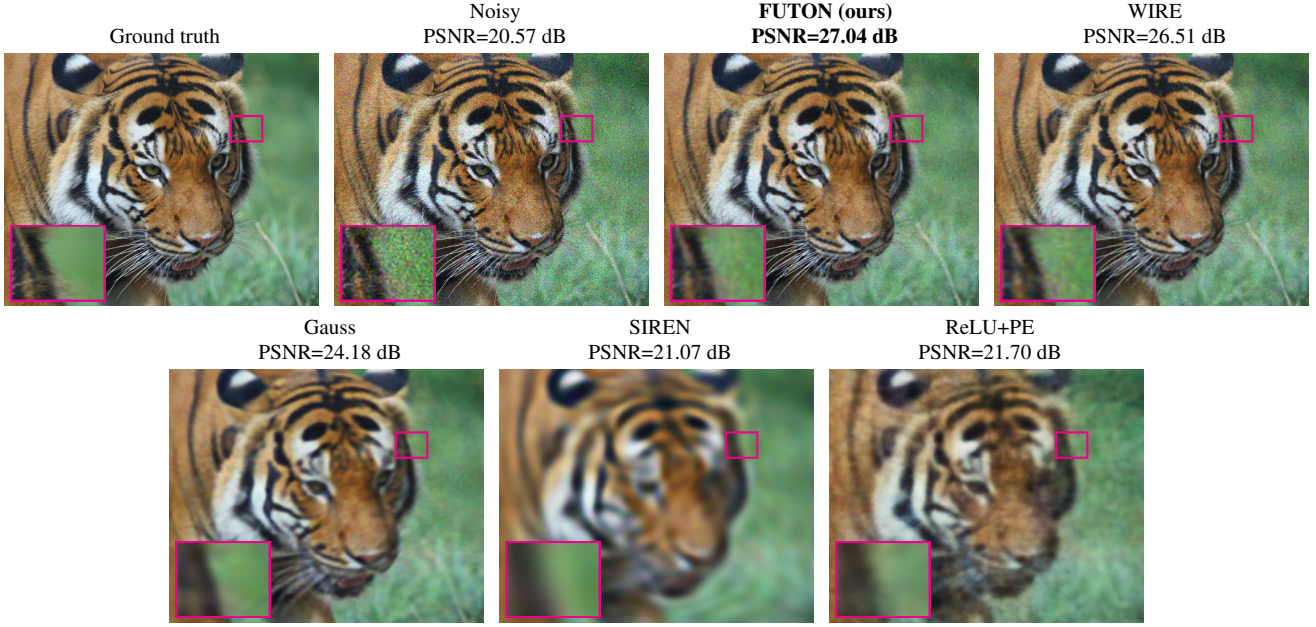


Figure 8. **Comparison on image denoising.** FUTON effectively reduces sensor noise while preserving image structure and details, achieving the highest reconstruction quality. The image is taken from the DIV2K dataset, 4 \times downsampled, and corrupted with sensor noise.

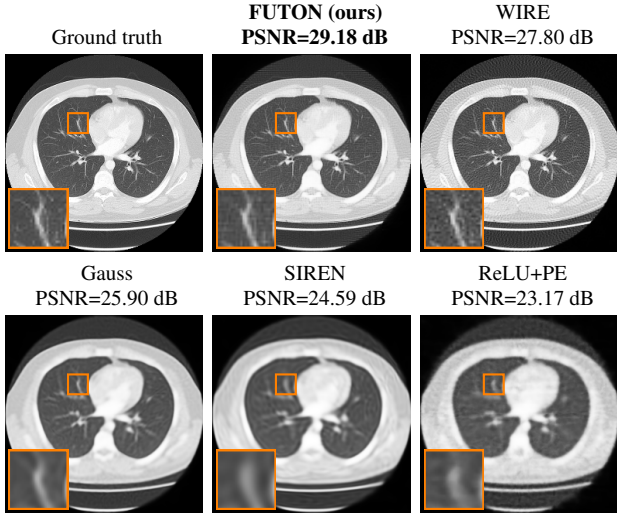


Figure 9. **Comparison on sparse-view CT reconstruction.** FUTON produces clearer anatomical structures with reduced streak artifacts from 150 projection angles. The CT scan is taken from Radiopedia and downsized to 256 \times 256 resolution.

high-frequency noise.

5.3.3. CT Reconstruction

CT reconstruction recovers 2D slices from Radon transform projections. We evaluate on a chest CT from Radiopedia downsized to 256 \times 256, simulating 150 projection angles uniformly over 180° (sparse-view protocol). We optimize in the sinogram domain, minimizing $\mathcal{L}_{\text{Radon}} =$

$\|\mathcal{R}(s) - \mathcal{R}(\hat{s})\|^2$, where \mathcal{R} is the Radon transform, ensuring reconstruction-projection consistency. We employ weight decay regularization with $\lambda = 4 \times 10^{-3}$ for FUTON and all baselines to prevent overfitting and train for 4000 epochs to allow sufficient convergence.

As shown in Figure 9, FUTON (with $R = K = 256$) achieves a PSNR of 29.18 dB, exceeding WIRE by 1.38 dB and outperforming Gauss (25.90 dB), SIREN (24.59 dB), and ReLU+PE (23.17 dB). FUTON produces clearer anatomical structures with reduced streak artifacts (characteristic of limited-angle tomographic reconstruction) and better-delineated lung and mediastinal structures. These results indicate effectiveness beyond natural images, with potential for computational imaging and medical diagnostics where reducing radiation dose while maintaining quality is paramount.

6. Conclusion

We presented FUTON, a structured INR that unifies generalized Fourier series with a low-rank CP decomposition of the coefficient tensor. This design addresses common limitations of MLP-based INRs (*e.g.*, slow convergence, overfitting, and poor extrapolation), while offering a linear-time forward pass and universal approximation in L^2 . FUTON leverages complementary inductive biases, where separable basis functions capture smoothness and periodicity, and low-rank parameterization organizes the spectrum.

Extensive experiments across diverse image and signal tasks validate the approach. For representation, FUTON delivers competitive or state-of-the-art quality while train-

ing substantially faster than strong baselines such as WIRE. For inverse problems, it generalizes well, improving single-image super-resolution over standard bilinear interpolation and denoising without artifacts. These findings position FUTON as a practical and reliable alternative to MLPs.

Promising directions include exploring alternative orthonormal bases (*e.g.*, learned adaptive bases) and tensor networks beyond CP (*e.g.*, Tucker, Tensor Train) for better trade-offs for specific signal classes. Applying FUTON to higher-dimensional tasks like video representation and neural radiance fields could also broaden its impact.

References

- [1] Eirikur Agustsson and Radu Timofte. NTIRE 2017 challenge on single image super-resolution: Dataset and study. In *CVPRW*, pages 126–135, 2017. 6
- [2] J Douglas Carroll and Jih-Jie Chang. Analysis of individual differences in multidimensional scaling via an N-way generalization of “Eckart-Young” decomposition. In *Psychometrika*, pages 283–319, 1970. 2, 3
- [3] Eric R. Chan, Connor Z. Lin, Matthew A. Chan, Koki Nagano, Boxiao Pan, Shalini De Mello, Orazio Gallo, Leonidas J. Guibas, Jonathan Tremblay, Sameh Khamis, Tero Karras, and Gordon Wetzstein. Efficient geometry-aware 3D generative adversarial networks. In *CVPR*, pages 16123–16133, 2022. 2
- [4] Anpei Chen, Zexiang Xu, Andreas Geiger, Jingyi Yu, and Hao Su. TensoRF: Tensorial radiance fields. In *ECCV*, pages 333–350, 2022. 2
- [5] Sara Fridovich-Keil, Giacomo Meanti, Frederik Rahbæk Wburg, Benjamin Recht, and Angjoo Kanazawa. K-Planes: Explicit radiance fields in space, time, and appearance. In *CVPR*, pages 12479–12488, 2023. 2
- [6] Amos Gropp, Lior Yariv, Niv Haim, Matan Atzmon, and Yaron Lipman. Implicit geometric regularization for learning shapes. In *ICML*, pages 3789–3799, 2020. 1, 2
- [7] Richard A Harshman. Foundations of the PARAFAC procedure: Models and conditions for an “explanatory” multimodal factor analysis. *UCLA Working Papers in Phonetics*, 16:1–84, 1970. 2, 3
- [8] Christopher J. Hillar and Lek-Heng Lim. Most tensor problems are NP-hard. *J. ACM*, 60(6), 2013. 3
- [9] Diederik P. Kingma and Jimmy Ba. Adam: A method for stochastic optimization. In *ICLR*, 2015. 4, 5
- [10] Kodak. Kodak lossless true color image suite. <http://r0k.us/graphics/kodak/>, 1993. 6
- [11] Tamara G. Kolda and Brett W. Bader. Tensor decompositions and applications. *SIAM Review*, 51(3):455–500, 2009. 1, 2, 4, 3
- [12] Ben Mildenhall, Pratul P Srinivasan, Matthew Tancik, Jonathan T Barron, Ravi Ramamoorthi, and Ren Ng. NeRF: Representing scenes as neural radiance fields for view synthesis. In *ECCV*, pages 405–421, 2020. 1, 2, 5
- [13] Jeong Joon Park, Peter Florence, Julian Straub, Richard Newcombe, and Steven Lovegrove. DeepSDF: Learning continuous signed distance functions for shape representation. In *CVPR*, pages 165–174, 2019. 1, 2
- [14] Keunhong Park, Utkarsh Sinha, Jonathan T Barron, Sofien Bouaziz, Dan B Goldman, Steven M Seitz, and Ricardo Martin-Brualla. Nerfies: Deformable neural radiance fields. In *ICCV*, pages 5865–5874, 2021. 2
- [15] Albert Pumarola, Enric Corona, Gerard Pons-Moll, and Francesc Moreno-Noguer. D-NeRF: Neural radiance fields for dynamic scenes. In *CVPR*, pages 10313–10322, 2021. 2
- [16] Nasim Rahaman, Aristide Baratin, Devansh Arpit, Felix Draxler, Min Lin, Fred Hamprecht, Yoshua Bengio, and Aaron Courville. On the spectral bias of neural networks. In *ICML*, pages 5301–5310, 2019. 1, 2
- [17] Sameera Ramasinghe and Simon Lucey. Beyond periodicity: Towards a unifying framework for activations in Coordinate-MLPs. In *ECCV*, pages 142–158, 2022. 1, 2, 3, 5
- [18] Vishwanath Saragadam, Daniel LeJeune, Jasper Tan, Guha Balakrishnan, Ashok Veeraraghavan, and Richard G Baraniuk. WIRE: Wavelet implicit neural representations. In *CVPR*, pages 18507–18516, 2023. 1, 2, 3, 5
- [19] Liyue Shen, John Pauly, and Lei Xing. NeRP: Implicit neural representation learning with prior embedding for sparsely sampled image reconstruction. *IEEE Trans. Neural Netw. Learn. Syst.*, 35(1):770–782, 2024. 1, 2
- [20] Vincent Sitzmann, Julien Martel, Alexander Bergman, David Lindell, and Gordon Wetzstein. Implicit neural representations with periodic activation functions. In *NeurIPS*, pages 7462–7473, 2020. 1, 2, 3, 5, 6
- [21] Elias M Stein and Rami Shakarchi. *Fourier analysis: an introduction*. Princeton University Press, 2011. 3
- [22] Yu Sun, Jiaming Liu, Mingyang Xie, Brendt Wohlberg, and Ulugbek S. Kamilov. COIL: Coordinate-based internal learning for imaging inverse problems. *IEEE Trans. Comput. Imaging*, 7:1400–1412, 2021. 2
- [23] Matthew Tancik, Pratul Srinivasan, Ben Mildenhall, Sara Fridovich-Keil, Nithin Raghavan, Utkarsh Singhal, Ravi Ramamoorthi, Jonathan Barron, and Ren Ng. Fourier features let networks learn high frequency functions in low dimensional domains. In *NeurIPS*, pages 7537–7547, 2020. 2
- [24] Ledyard R. Tucker. Some mathematical notes on three-mode factor analysis. *Psychometrika*, 31(3):279–311, 1966. 2
- [25] Sai Karthikeya Vemuri, Tim Büchner, and Joachim Denzler. F-INR: Functional tensor decomposition for implicit neural representations. *arXiv preprint arXiv:2503.21507*, 2025. 2
- [26] Yinbo Wang, Ceyuan Zhou, and Qifeng Chen. Learning continuous image representation with local implicit image function. In *CVPR*, pages 8624–8634, 2021. 2
- [27] Ruyi Zha, Yanhao Zhang, and Hongdong Li. NAF: Neural attenuation fields for sparse-view CBCT reconstruction. In *MICCAI*, pages 442–452, 2022. 1, 2

FUTON: Fourier Tensor Network for Implicit Neural Representations

Supplementary Material

7. L^2 Space

FUTON’s theoretical foundation relies on generalized Fourier series in L^2 spaces (Section 3.2). We provide formal definitions of the L^2 space and related concepts.

Definition 2 (L^2 Space). Let $\mathbb{X} \subseteq \mathbb{R}^D$ for some $D \in \mathbb{N}$. The Hilbert space $L^2(\mathbb{X})$ consists of **square-integrable** functions on \mathbb{X} , where $f \in L^2(\mathbb{X})$ if and only if

$$\int_{\mathbb{X}} |f(\mathbf{x})|^2 d\mathbf{x} < \infty. \quad (13)$$

For instance, $L^2([0, 1]^C)$ denotes the space of square-integrable functions on the C -dimensional unit hypercube.

Definition 3 (L^2 Inner Product). For $f, g \in L^2(\mathbb{X})$, the inner product is defined as

$$\langle f, g \rangle_{L^2} \triangleq \int_{\mathbb{X}} f(\mathbf{x})g(\mathbf{x}) d\mathbf{x}. \quad (14)$$

Definition 4 (L^2 Norm). For $f \in L^2(\mathbb{X})$, the norm is defined as

$$\|f\|_{L^2} \triangleq \sqrt{\langle f, f \rangle_{L^2}}. \quad (15)$$

Definition 5 (L^2 Convergence). A sequence $(f_k)_{k \in \mathbb{N}_0}$ in $L^2(\mathbb{X})$ is said to converge in $L^2(\mathbb{X})$ to a function $f \in L^2(\mathbb{X})$ if $\lim_{k \rightarrow \infty} \|f_k - f\|_{L^2} = 0$, denoted as $f_k \xrightarrow{L^2} f$.

Definition 6 (L^2 Orthonormality). A set of functions $\{\varphi_k\}_{k \in \mathbb{I}} \subseteq L^2(\mathbb{X})$ is **orthonormal** in $L^2(\mathbb{X})$ if $\langle \varphi_k, \varphi_\ell \rangle_{L^2} = \delta_{k\ell}$ for all $k, \ell \in \mathbb{I}$, where $\delta_{k\ell}$ is the Kronecker delta (1 if $k = \ell$, 0 otherwise).

Definition 7 (L^2 Density). A subset $\mathbb{D} \subseteq L^2(\mathbb{X})$ is said to be **dense** in $L^2(\mathbb{X})$ if for every function $f \in L^2(\mathbb{X})$ there exists a sequence $(f_k)_{k \in \mathbb{N}_0}$ in \mathbb{D} such that $f_k \xrightarrow{L^2} f$. In other words, any function in $L^2(\mathbb{X})$ can be approximated arbitrarily closely by functions from \mathbb{D} .

Definition 8 (L^2 Completeness). A set of functions is said to be **complete** in $L^2(\mathbb{X})$ if its **span** is **dense** in $L^2(\mathbb{X})$. Formally, $\{\varphi_k\}_{k \in \mathbb{N}} \subseteq L^2(\mathbb{X})$ is complete if for every function $f \in L^2(\mathbb{X})$, there exists coefficients $w_1, \dots, w_K \in \mathbb{R}$ such that the partial sum $s_K = \sum_{k=1}^K w_k \varphi_k$ converges to f in $L^2(\mathbb{X})$ as $K \rightarrow \infty$. In other words, any function in $L^2(\mathbb{X})$ can be approximated arbitrarily closely by a finite linear combination of functions from $\{\varphi_k\}_{k \in \mathbb{N}}$.

Definition 9 (L^2 Orthonormal Basis). A set of functions $\{\varphi_k\}_{k \in \mathbb{N}_0} \subseteq L^2(\mathbb{X})$ is said to be an **orthonormal basis (ONB)** for $L^2(\mathbb{X})$ if it is both **orthonormal** and **complete** in $L^2(\mathbb{X})$.

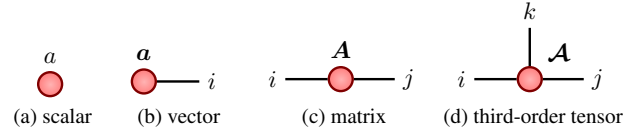


Figure 10. **Tensor diagram notation.** Graphical representation of tensors with different orders: (a) scalar (0th-order), (b) vector (1st-order), (c) matrix (2nd-order), and (d) third-order tensor. In tensor diagrams, tensors are represented as nodes (shapes) with edges (lines) denoting indices. Dangling edges represent open (uncontracted) indices.

8. Tensor Networks

8.1. Tensor Diagram Notation

A tensor is a multidimensional array of numbers. An M -th-order tensor $\mathcal{A} \in \mathbb{R}^{I_1 \times I_2 \times \dots \times I_M}$ is a multi-dimensional array where the m th mode (dimension or index) has size I_m . Special cases include scalars ($M = 0$), vectors ($M = 1$), and matrices ($M = 2$).

Index Contraction. An *index contraction* sums over all values of shared indices between tensors. For example, matrix multiplication

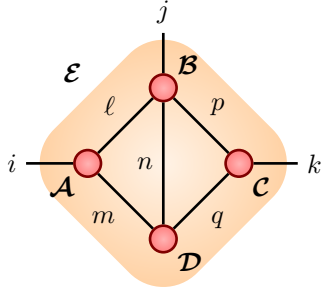
$$c_{ij} = \sum_{k=1}^K a_{ik} b_{kj} \quad (16)$$

contracts index k over K values. More complex contractions involve multiple tensors and indices:

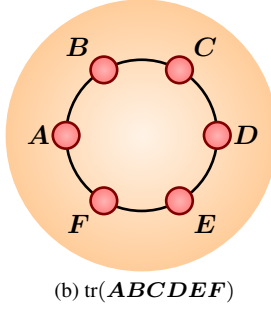
$$e_{ijk} = \sum_{\ell,m,n,p,q=1}^R a_{i\ell m} b_{j\ell n} c_{kpq} d_{mnq}. \quad (17)$$

Indices that remain after contraction (i, j, k) are called *open indices*. A *tensor network* is a set of tensors with indices contracted according to a specified pattern.

Tensor Diagrams. *Tensor diagrams* provide powerful graphical notation for tensor operations. As shown in Figure 10, tensors are represented as nodes with edges corresponding to indices. Edges connecting tensors represent contracted indices, while dangling edges represent open indices. This notation simplifies understanding of complex tensor operations and is used throughout the main paper (see Figures 2 and 3).



$$(a) e_{ijk} = \sum_{\ell, m, n, p, q=1}^R a_{i\ell m} b_{j\ell np} c_{kpq} d_{mna}$$



$$(b) \text{tr}(\mathbf{ABCDEF})$$

Figure 11. **Tensor diagram examples.** (a) Complex tensor network from (17) with multiple contracted indices. Edges connecting different nodes represent shared indices that are summed over. (b) Trace of matrix product $\text{tr}(\mathbf{ABCDEF})$ represented as a ring diagram, where the cyclic property becomes visually apparent, *i.e.*, any rotation of the ring yields the same value.

Figure 11a illustrates tensor diagrams for the complex contraction in (17). As another example of complex calculations, the trace of the product of six matrices can be represented by a simple ring-like diagram as seen in Figure 11b. From this tensor diagram, the cyclic property of the trace becomes clear. This is a simple example of why tensor diagrams are advantageous. Tensor diagrams make structural properties visually apparent and are particularly useful for understanding operations like those in FUTON (see Figures 2 and 3 in the main paper).

Many matrix and tensor operations perform some form of tensor network contraction, and hence, can be represented graphically using tensor diagrams. Figure 12 illustrates the tensor diagrams of some basic operations.

8.2. Basic Tensor Operations

Definition 10 (Fiber). *A mode- m fiber of a tensor $\mathcal{A} \in \mathbb{R}^{I_1 \times I_2 \times \dots \times I_M}$ is a vector obtained by fixing every index except the m th, *i.e.*, $\mathcal{A}_{i_1 \dots i_{m-1} : i_{m+1} \dots i_M}$ for fixed indices $i_j \in \{1, \dots, I_j\}$ where $j \neq m$.*

Definition 11 (Matricization). *The mode- m matricization (or unfolding) of a tensor $\mathcal{A} \in \mathbb{R}^{I_1 \times I_2 \times \dots \times I_M}$ is defined*

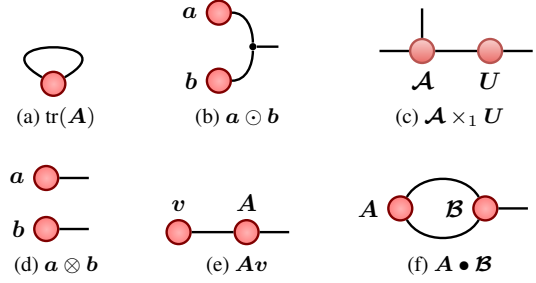


Figure 12. **Tensor diagrams of basic operations.** (a) matrix trace; (b) Hadamard product, used in (10); (c) mode-1 product; (d) tensor product, used in (6) and (8); (e) matrix-vector multiplication, used in (11) and (9); and (f) generalized dot product, used in (7).

as the matrix $\mathcal{A}_{(m)} \in \mathbb{R}^{I_m \times (I_1 \dots I_{m-1} I_{m+1} \dots I_M)}$ obtained by stacking all mode- m fibers of \mathcal{A} along the columns, arranged in lexicographical order.

Definition 12 (Hadamard Product). *The Hadamard product $\mathcal{C} = \mathcal{A} \odot \mathcal{B}$ of equally-sized tensors $\mathcal{A}, \mathcal{B} \in \mathbb{R}^{I_1 \times \dots \times I_M}$ performs elementwise multiplication:*

$$c_{i_1 \dots i_M} = a_{i_1 \dots i_M} b_{i_1 \dots i_M}. \quad (18)$$

Figure 12b illustrates the tensor diagram for the Hadamard product of two vectors.

Definition 13 (Inner Product). *The inner product (or dot product) of equally-sized tensors $\mathcal{A}, \mathcal{B} \in \mathbb{R}^{I_1 \times \dots \times I_M}$ is*

$$\langle \mathcal{A}, \mathcal{B} \rangle \triangleq \sum_{i_1, \dots, i_M} a_{i_1 \dots i_M} b_{i_1 \dots i_M}. \quad (19)$$

The inner product is a special case of the generalized dot product (Definition 1) where both tensors have identical shapes.

Definition 14 (Tensor Product). *The tensor product $\mathcal{C} = \mathcal{A} \otimes \mathcal{B}$ of tensors $\mathcal{A} \in \mathbb{R}^{I_1 \times \dots \times I_M}$ and $\mathcal{B} \in \mathbb{R}^{J_1 \times \dots \times J_N}$ yields $\mathcal{C} \in \mathbb{R}^{I_1 \times \dots \times I_M \times J_1 \times \dots \times J_N}$ with elements*

$$c_{i_1 \dots i_M j_1 \dots j_N} = a_{i_1 \dots i_M} b_{j_1 \dots j_N}. \quad (20)$$

Figure 12d illustrates the tensor diagram for the tensor product of two vectors.

Definition 15 (Tensor-Matrix Product). *The mode- m product of a tensor $\mathcal{A} \in \mathbb{R}^{I_1 \times I_2 \times \dots \times I_M}$ and a matrix $\mathcal{U} \in \mathbb{R}^{J \times I_m}$ is the tensor*

$$\mathcal{C} = \mathcal{A} \times_m \mathcal{U} \in \mathbb{R}^{I_1 \times \dots \times I_{m-1} \times J \times I_{m+1} \times \dots \times I_M} \quad (21)$$

with elements

$$c_{i_1 \dots i_{m-1} j i_{m+1} \dots i_M} = \sum_{i_m=1}^{I_M} a_{i_1 \dots i_M} U_{ji_m}. \quad (22)$$

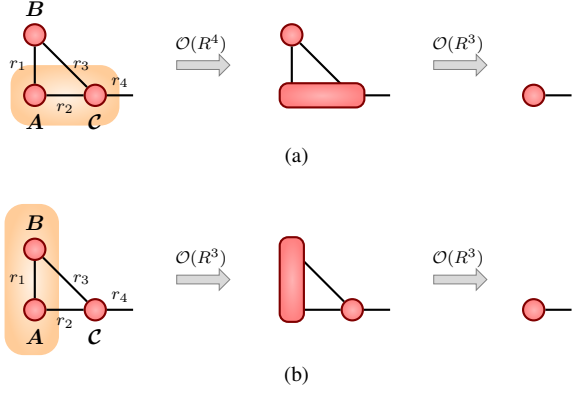


Figure 13. **Sequential contraction of a tensor network.** All modes are of size R . In (a), the matrix A and the tensor C are first contracted (mode- m product), then the resulting tensor is contracted with the matrix B , requiring $\mathcal{O}(R^4)$ operations in total. In (b), the matrices A and B are first contracted (multiplied), then the resulting matrix is contracted with the tensor C , requiring $\mathcal{O}(R^3)$ operations in total.

Figure 12c illustrates the tensor diagram of the mode-1 product of a third-order tensor and a matrix.

An equivalent matrix representation of the mode- m product is $C_{(m)} = \mathbf{U} A_{(m)}$, which allows us to employ established fast matrix multiplications when dealing with very large-scale tensors.

8.3. Contraction Order

The computational cost of tensor network contractions depends critically on the order in which indices are contracted. Figure 13 illustrates this: contracting A and C first (Figure 13a) requires $\mathcal{O}(R^4)$ operations, while contracting A and B first (Figure 13b) requires only $\mathcal{O}(R^3)$ operations. This principle is crucial for FUTON’s linear complexity (see Section 4.2).

8.4. Canonical Polyadic Decomposition

Definition 16 (Rank-1 Tensor). A rank-1 tensor $\mathbf{A} \in \mathbb{R}^{I_1 \times I_2 \times \dots \times I_M}$ is a tensor that can be expressed as the tensor product of nonzero vectors $\{\mathbf{u}^{(m)} \in \mathbb{R}^{I_m}\}_{m=1}^M$:

$$\mathbf{A} = \mathbf{u}^{(1)} \otimes \mathbf{u}^{(2)} \otimes \dots \otimes \mathbf{u}^{(M)}. \quad (23)$$

Equivalently, the elements of \mathbf{A} satisfy

$$a_{i_1 \dots i_M} = u_{i_1}^{(1)} u_{i_2}^{(2)} \dots u_{i_M}^{(M)}. \quad (24)$$

Definition 17 (Rank). The rank of a tensor \mathbf{A} , denoted by $\text{rank}(\mathbf{A})$, is the minimal number of rank-1 tensors that sum to \mathbf{A} .

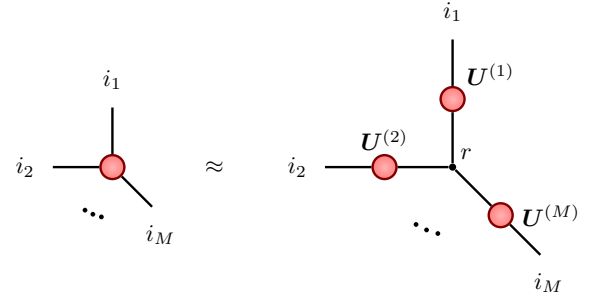


Figure 14. **Tensor diagram of CP decomposition.**

Definition 18 (CP Decomposition). Canonical polyadic (CP) decomposition [2, 7] represents a tensor $\mathbf{A} \in \mathbb{R}^{I_1 \times \dots \times I_M}$ as a sum of R rank-1 tensors:

$$\mathbf{A} = \sum_{r=1}^R \mathbf{u}_r^{(1)} \otimes \mathbf{u}_r^{(2)} \otimes \dots \otimes \mathbf{u}_r^{(M)}, \quad (25)$$

where $\mathbf{u}_r^{(m)} \in \mathbb{R}^{I_m}$ are factor vectors, and R is the CP rank. Factor matrices $\mathbf{U}^{(m)} = [\mathbf{u}_1^{(m)} \mid \dots \mid \mathbf{u}_R^{(m)}] \in \mathbb{R}^{I_m \times R}$ collect the vectors for mode m .

Figure 14 shows the tensor diagram for CP decomposition, which can be understood by expressing (25) element-wise:

$$a_{i_1 \dots i_M} = \sum_{r=1}^R \prod_{m=1}^M u_{i_m r}^{(m)}. \quad (26)$$

The CP decomposition (25) can be written in terms of matricization as:

$$\mathbf{A}_{(m)} = \mathbf{U}^{(m)} \mathbf{V}^{(m)\top}, \quad (27)$$

where $\mathbf{V}^{(m)} = [\mathbf{v}_1^{(m)} \mid \dots \mid \mathbf{v}_R^{(m)}] \in \mathbb{R}^{(\prod_{j \neq m} I_j) \times R}$, and $\mathbf{v}_r^{(m)} = \text{vec}(\otimes_{j \neq m} \mathbf{u}_r^{(j)})$ for $r \in \{1, \dots, R\}$.

It is important to distinguish between the CP rank R in (25) and the (exact) rank $\text{rank}(\mathbf{A})$ from Definition 17. The CP rank specifies the number of rank-1 components in an approximate decomposition, while the (exact) rank is the minimal number required for exact representation. When $R = \text{rank}(\mathbf{A})$ in (25), the result is called a *tensor rank decomposition* or *minimal CP decomposition*. However, determining the (exact) rank is NP-hard in general [8]. In practice, approximate low-rank CP decompositions are computed using iterative methods such as alternating least squares or gradient-based optimization Kolda and Bader [11], where R is chosen based on computational constraints and approximation accuracy.

8.5. Tensor Networks as a Computational Tool

Low-rank tensor representations enable efficient computation with high-dimensional data. Storing an M th-order tensor with each mode of size I requires I^M elements, which

grows exponentially in M . In contrast, CP decomposition with rank R requires only $\mathcal{O}(MIR)$ parameters, reducing storage and computational costs dramatically.

Example 1 (Rank-1 Inner Product). *Consider computing the inner product of two M th-order tensors $\mathbf{A}, \mathbf{B} \in \mathbb{R}^{I \times I \times \dots \times I}$. Direct computation using Equation (19) requires $\mathcal{O}(I^M)$ operations, which becomes intractable for large M . However, when \mathbf{A} and \mathbf{B} are rank-1 tensors, i.e. $\mathbf{A} = \mathbf{a}^{(1)} \otimes \mathbf{a}^{(2)} \otimes \dots \otimes \mathbf{a}^{(M)}$ and $\mathbf{B} = \mathbf{b}^{(1)} \otimes \mathbf{b}^{(2)} \otimes \dots \otimes \mathbf{b}^{(M)}$, the inner product decomposes as*

$$\begin{aligned} \langle \mathbf{A}, \mathbf{B} \rangle &= \sum_{i_1, \dots, i_M=1}^I a_{i_1 \dots i_M} b_{i_1 \dots i_M} \\ &= \sum_{i_1, \dots, i_M=1}^I \left[\prod_{m=1}^M a_{i_m}^{(m)} \right] \left[\prod_{m=1}^M b_{i_m}^{(m)} \right] \\ &= \prod_{m=1}^M \left[\sum_{i_m=1}^I a_{i_m}^{(m)} b_{i_m}^{(m)} \right] \\ &= \prod_{m=1}^M \langle \mathbf{a}^{(m)}, \mathbf{b}^{(m)} \rangle. \end{aligned}$$

This requires only $\mathcal{O}(MI)$ operations by computing the mode-wise inner products $\langle \mathbf{a}^{(m)}, \mathbf{b}^{(m)} \rangle$ first, then multiplying the results—an exponential speedup. More generally, representing high-order tensors with low-rank tensor networks (e.g. CP decomposition) and executing contractions in optimal order (as detailed in Section 8.3) dramatically reduces computational complexity in numerous machine learning applications.

9. Proof of Theorem 1

Orthonormality. Let $\mathbf{k}, \ell \in \mathbb{N}_0^C$. By Fubini's theorem and the separable definition of $\phi_{\mathbf{k}}$ in (2), the inner product decomposes over dimensions:

$$\begin{aligned} \langle \phi_{\mathbf{k}}, \phi_{\ell} \rangle_{L^2} &= \int_{[0,1]^C} \phi_{\mathbf{k}}(\mathbf{x}) \phi_{\ell}(\mathbf{x}) d\mathbf{x} \\ &= \int_{[0,1]^C} \left[\prod_{c=1}^C \varphi_{k_c}(x_c) \right] \left[\prod_{c=1}^C \varphi_{\ell_c}(x_c) \right] d\mathbf{x} \\ &= \prod_{c=1}^C \int_0^1 \varphi_{k_c}(x_c) \varphi_{\ell_c}(x_c) dx_c \\ &= \prod_{c=1}^C \delta_{k_c \ell_c} = \delta_{\mathbf{k} \ell}. \end{aligned} \tag{28}$$

The penultimate equality follows from the orthonormality of the one-dimensional basis $\{\varphi_k\}_{k \in \mathbb{N}_0}$.

Completeness. We prove the completeness by the *orthogonal complement* criterion. Let $f \in L^2([0,1]^C)$ satisfy $\langle f, \phi_{\mathbf{k}} \rangle_{L^2} = 0$ for all $\mathbf{k} \in \mathbb{N}_0^C$. We show $f = 0$ almost everywhere (i.e., $\|f\|_{L^2} = 0$).

We argue by induction on C . The case $C = 1$ holds because $\{\varphi_k\}_{k \in \mathbb{N}_0}$ is an ONB in $L^2([0,1])$ by assumption. Assume the claim holds for dimension $C - 1$. For $k_1 \in \mathbb{N}_0$, define

$$h_{k_1}(\mathbf{x}_{-1}) \triangleq \int_0^1 f(x_1, \mathbf{x}_{-1}) \varphi_{k_1}(x_1) dx_1, \tag{29}$$

where $\mathbf{x}_{-1} = (x_2, \dots, x_C)$ is the vector of all coordinates except x_1 . By the Cauchy–Schwarz inequality applied in the x_1 -coordinate, for almost every $\mathbf{x}_{-1} \in [0,1]^{C-1}$,

$$\begin{aligned} |h_{k_1}(\mathbf{x}_{-1})|^2 &= \left| \int_0^1 f(x_1, \mathbf{x}_{-1}) \varphi_{k_1}(x_1) dx_1 \right|^2 \\ &\leq \left(\int_0^1 |f(\mathbf{x})|^2 dx_1 \right) \left(\int_0^1 |\varphi_{k_1}(x_1)|^2 dx_1 \right) \\ &= \int_0^1 |f(\mathbf{x})|^2 dx_1, \end{aligned} \tag{30}$$

since $\{\varphi_k\}_{k \in \mathbb{N}_0}$ is orthonormal in $L^2([0,1])$. Integrating over \mathbf{x}_{-1} and applying Fubini's theorem yields

$$\begin{aligned} \|h_{k_1}\|_{L^2}^2 &= \int_{[0,1]^{C-1}} |h_{k_1}(\mathbf{x}_{-1})|^2 d\mathbf{x}_{-1} \\ &\leq \int_{[0,1]^C} |f(\mathbf{x})|^2 d\mathbf{x} < \infty, \end{aligned} \tag{31}$$

hence $h_{k_1} \in L^2([0,1]^{C-1})$. For any $\mathbf{k}_{-1} = (k_2, \dots, k_C) \in \mathbb{N}_0^{C-1}$,

$$\begin{aligned} 0 &= \langle f, \phi_{(k_1, \mathbf{k}_{-1})} \rangle_{L^2} \\ &= \int_{[0,1]^{C-1}} h_{k_1}(\mathbf{x}_{-1}) \prod_{c=2}^C \varphi_{k_c}(x_c) d\mathbf{x}_{-1}. \end{aligned} \tag{32}$$

Hence h_{k_1} is orthogonal in $L^2([0,1]^{C-1})$ to the set $\{\prod_{c=2}^C \varphi_{k_c}\}_{\mathbf{k}_{-1} \in \mathbb{N}_0^{C-1}}$, which is an ONB by the induction hypothesis; therefore $h_{k_1} = 0$ almost everywhere for every $k_1 \in \mathbb{N}_0$.

For almost every \mathbf{x}_{-1} , the slice $x_1 \mapsto f(x_1, \mathbf{x}_{-1})$ has all one-dimensional Fourier coefficients zero:

$$\int_0^1 f(x_1, \mathbf{x}_{-1}) \varphi_{k_1}(x_1) dx_1 = 0, \quad \forall k_1 \in \mathbb{N}_0. \tag{33}$$

By completeness of $\{\varphi_k\}_{k \in \mathbb{N}_0}$ in $L^2([0,1])$, it follows that $f(\cdot, \mathbf{x}_{-1}) = 0$ in $L^2([0,1])$ for almost every \mathbf{x}_{-1} , and thus $f = 0$ almost everywhere on $[0,1]^C$. \square

10. Proof of Theorem 2

It suffices to prove convergence for each component s_d independently. Fix $d \in \{1, \dots, D\}$ and let $s_d \in L^2([0, 1]^C)$ be arbitrary. By Theorem 1, the separable family $\{\phi_k\}_{k \in \mathbb{N}_0^C}$ from (2) forms an ONB for $L^2([0, 1]^C)$.

For $K \in \mathbb{N}$, recall $\mathbb{K} = \{0, \dots, K-1\}^C$ and define the finite-dimensional subspace

$$\mathbb{V}_K \triangleq \text{span}\{\phi_k : k \in \mathbb{K}\}. \quad (34)$$

Clearly $\mathbb{V}_K \subseteq \mathbb{V}_{K+1}$ for all K , and by completeness of the ONB, $\bigcup_{K \geq 1} \mathbb{V}_K$ is dense in $L^2([0, 1]^C)$.

Let $P_K : L^2([0, 1]^C) \rightarrow \mathbb{V}_K$ denote the orthogonal projection onto \mathbb{V}_K . Since $\{\phi_k\}_{k \in \mathbb{K}}$ is an orthonormal set, the projection has the Fourier expansion

$$P_K(s_d) = \sum_{k \in \mathbb{K}} \langle s_d, \phi_k \rangle_{L^2} \phi_k. \quad (35)$$

Comparing with (3) and (4), we identify $P_K(s_d) = \hat{s}_{d,K}$.

To establish L^2 convergence, fix $\varepsilon > 0$. By density, there exists a finite linear combination $f = \sum_{k \in \mathbb{J}} c_k \phi_k$ for some finite index set $\mathbb{J} \subset \mathbb{N}_0^C$ such that $\|s_d - f\|_{L^2} < \varepsilon/2$. Since \mathbb{J} is finite, there exists $K_0 \in \mathbb{N}$ sufficiently large that $\mathbb{J} \subseteq \mathbb{K}$ for all $K \geq K_0$; hence $f \in \mathbb{V}_K$ for all $K \geq K_0$.

For $K \geq K_0$, the best approximation property of orthogonal projections (i.e., $P_K(s_d)$ minimizes $\|s_d - v\|_{L^2}$ over all $v \in \mathbb{V}_K$) yields

$$\|s_d - \hat{s}_{d,K}\|_{L^2} = \|s_d - P_K(s_d)\|_{L^2} \leq \|s_d - f\|_{L^2} < \frac{\varepsilon}{2} < \varepsilon,$$

where the inequality holds since $f \in \mathbb{V}_K$. Since $\varepsilon > 0$ was arbitrary, we conclude $\|s_d - \hat{s}_{d,K}\|_{L^2} \rightarrow 0$ as $K \rightarrow \infty$.

Since the choice of $d \in \{1, \dots, D\}$ was arbitrary, the convergence holds for all components, yielding $\hat{s}_K \xrightarrow{L^2} s$ as $K \rightarrow \infty$. \square

11. Proof of Theorem 3

Lemma 1 (Rank Upper Bound). *Let $\mathcal{A} \in \mathbb{R}^{I_1 \times \dots \times I_M}$ be an M th-order tensor. Then*

$$\text{rank}(\mathcal{A}) \leq \min_{1 \leq m \leq M} \prod_{\substack{j=1 \\ j \neq m}}^M I_j. \quad (36)$$

Proof. Fix $m \in \{1, \dots, M\}$. We construct an explicit rank-1 decomposition with at most $\prod_{j \neq m} I_j$ terms by expanding in canonical bases.

Let $\mathbf{e}_{i_j}^{(j)} \in \mathbb{R}^{I_j}$ denote the i_j th standard basis vector, i.e., $[\mathbf{e}_{i_j}^{(j)}]_k = \delta_{i_j k}$. Any tensor \mathcal{A} admits the expansion

$$\mathcal{A} = \sum_{i_1=1}^{I_1} \dots \sum_{i_M=1}^{I_M} a_{i_1 \dots i_M} \mathbf{e}_{i_1}^{(1)} \otimes \dots \otimes \mathbf{e}_{i_M}^{(M)}. \quad (37)$$

Define the multi-index $\mathbf{i}_{-m} \triangleq (i_1, \dots, i_{m-1}, i_{m+1}, \dots, i_M) \in \prod_{j \neq m} \{1, \dots, I_j\}$. Reordering the summations in (37) and factoring out the mode- m sum yields

$$\begin{aligned} \mathcal{A} &= \sum_{\mathbf{i}_{-m}} \sum_{i_m=1}^{I_m} a_{i_1 \dots i_M} \mathbf{e}_{i_m}^{(m)} \otimes \left(\bigotimes_{j \neq m} \mathbf{e}_{i_j}^{(j)} \right) \\ &= \sum_{\mathbf{i}_{-m}} \underbrace{\left(\sum_{i_m=1}^{I_m} a_{i_1 \dots i_M} \mathbf{e}_{i_m}^{(m)} \right)}_{\mathbf{a}_{\mathbf{i}_{-m}}^{(m)}} \otimes \left(\bigotimes_{j \neq m} \mathbf{e}_{i_j}^{(j)} \right). \end{aligned} \quad (38)$$

Here $\mathbf{a}_{\mathbf{i}_{-m}}^{(m)} \in \mathbb{R}^{I_m}$ is the mode- m fiber of \mathcal{A} at index \mathbf{i}_{-m} (Definition 10), with components $[\mathbf{a}_{\mathbf{i}_{-m}}^{(m)}]_{i_m} = a_{i_1 \dots i_M}$. Each summand in (38) is rank-1 (Definition 16) since it is the tensor product of M vectors. The sum runs over $\prod_{j \neq m} I_j$ distinct values of \mathbf{i}_{-m} , so (38) expresses \mathcal{A} as a sum of at most $\prod_{j \neq m} I_j$ rank-1 tensors. By Definition 17, $\text{rank}(\mathcal{A}) \leq \prod_{j \neq m} I_j$. Since $m \in \{1, \dots, M\}$ was arbitrary, taking the minimum over all modes yields (36). \square

Proof of Theorem 3. Fix $\varepsilon > 0$. By Theorem 2, for each component $d \in \{1, \dots, D\}$ there exists $K_d \in \mathbb{N}$ such that for all $K \geq K_d$, the truncated generalized Fourier series $\hat{s}_{d,K}$ in (3) satisfies $\|s_d - \hat{s}_{d,K}\|_{L^2} < \varepsilon$. Let $K_0 \triangleq \max_d K_d$ and fix any $K \geq K_0$. Then $\|s_d - \hat{s}_{d,K}\|_{L^2} < \varepsilon$ holds simultaneously for all d .

For this K , collect the Fourier coefficients $w_d^{(k)}$ from (4) into the $(C+1)$ st-order weight tensor $\mathcal{W} \in \mathbb{R}^{K^{C+1} \times D}$ so that $\hat{s}_K(\mathbf{x}) = \Phi(\mathbf{x}) \bullet \mathcal{W}$ by (7), with Φ defined in (6). Applying Lemma 1 to \mathcal{W} (of sizes $I_1 = \dots = I_C = K$ and $I_{C+1} = D$) yields

$$\text{rank}(\mathcal{W}) \leq \min\{K^C, K^{C-1}D\} = K^{C-1} \min\{K, D\}. \quad (39)$$

Hence \mathcal{W} admits a CP decomposition of the form (8) with some rank $R \leq K^{C-1} \min\{K, D\}$ and factor matrices $\{\mathbf{U}^{(c)}\}_{c=1}^C, \mathbf{V}$. Substituting this decomposition together with (6) into (7) and regrouping terms gives exactly the FUTON computation (9)–(11). Therefore $s^{\text{futon}}(\mathbf{x}) \equiv \hat{s}_K(\mathbf{x})$, and for the chosen K and corresponding R and factors

$$\|s_d - s_d^{\text{futon}}\|_{L^2} = \|s_d - \hat{s}_{d,K}\|_{L^2} < \varepsilon, \quad \forall d \in \{1, \dots, D\}. \quad (40)$$

This establishes the theorem. \square

12. Training Efficiency Analysis

We analyze FUTON's training efficiency by measuring convergence speed in both wall-clock time and iteration count. This separates per-iteration computational cost from optimization efficiency, providing insight into the architectural advantages of FUTON's tensor network parameterization.

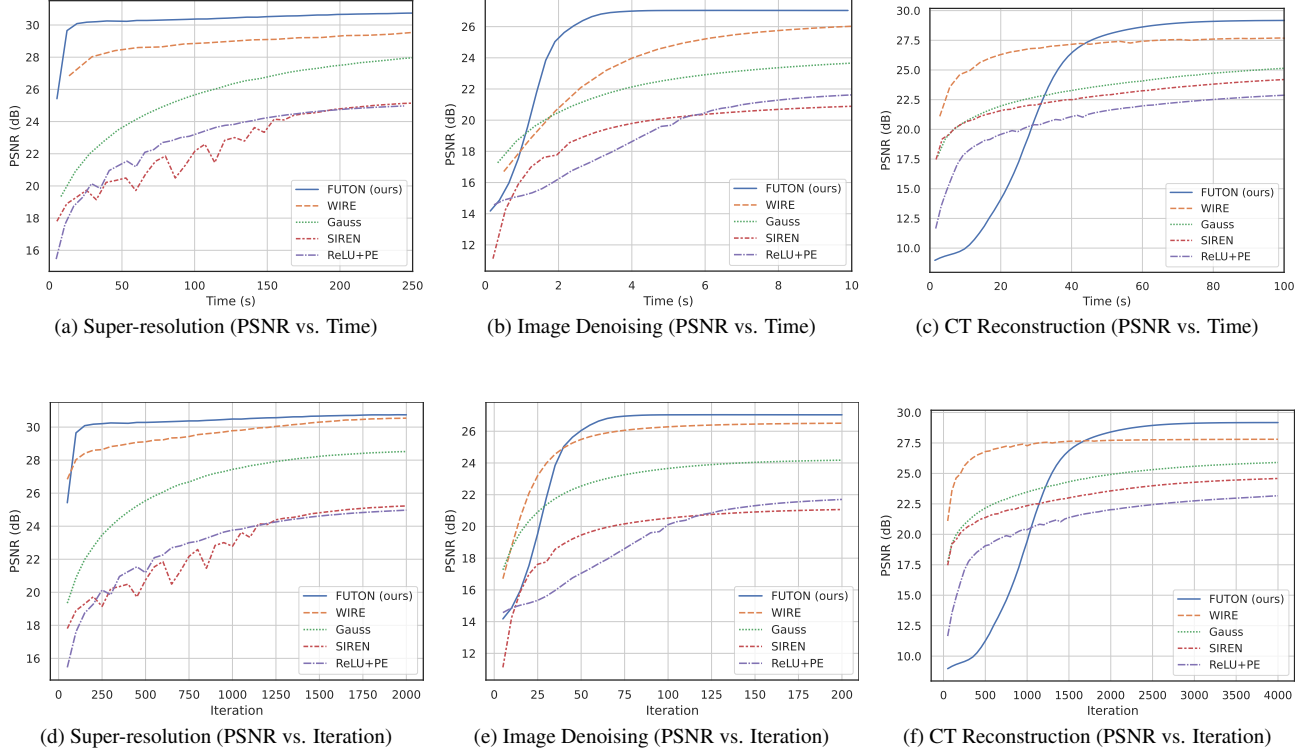


Figure 15. **Learning speed on inverse problems.** We compare the convergence of FUTON against baseline methods on three tasks: (a, d) super-resolution, (b, e) image denoising, and (c, f) CT reconstruction. The top row shows PSNR as a function of wall-clock training time, while the bottom row plots PSNR against the number of training iterations. In all experiments, FUTON converges significantly faster and reaches a higher PSNR, underscoring its efficiency and effectiveness for inverse problems.

Figure 15 presents convergence curves for super-resolution, image denoising, and CT reconstruction. The top row (Figures 15a to 15c) plots PSNR versus wall-clock time, while the bottom row (Figures 15d to 15f) plots PSNR versus iteration count.

Computational Efficiency. FUTON demonstrates superior wall-clock performance across all tasks. On super-resolution, FUTON reaches 30 dB in approximately 10s compared to over 25s for WIRE. For image denoising, FUTON achieves 27 dB in under 20s, while WIRE requires approximately 60s—a 3× speedup. The largest gains occur in CT reconstruction, where FUTON reaches 29 dB in 50s versus over 100s for WIRE, representing a 2× speedup. Periodic activation baselines (SIREN, Gauss) exhibit slower convergence and lower asymptotic PSNR, while ReLU+PE fails to converge effectively.

Optimization Landscape and Training Behavior. When measured by iteration count, FUTON maintains its advantage (Figures 15d to 15f), indicating favorable optimization

properties independent of per-iteration cost. The CP decomposition (Equation (9)) decouples learning of global spectral structure via low-rank components from local refinements via high-frequency coefficients, enabling efficient gradient-based optimization. Conversely, MLP-based INRs require coordinated layer-wise updates to modify global properties, often resulting in slow convergence [20]. add that FUTON has a shallow structure, yet higher expressiveness, and justify the training behavior in figure 5.

13. Ablation Studies

We ablate FUTON’s main design choices: CP rank R , number of basis functions K , and the one-dimensional basis $\varphi(\cdot)$. Unless stated otherwise, we fit `kodim17` from the Kodak dataset for 2000 epochs and report reconstruction quality (PSNR, SSIM) and inference speed (img/s). The default configuration uses $R = K = 512$ with the cosine basis (Equation (1)).

Rank (R). The CP rank R in (9) controls the expressiveness of FUTON’s low-rank weight tensor. Figure 16

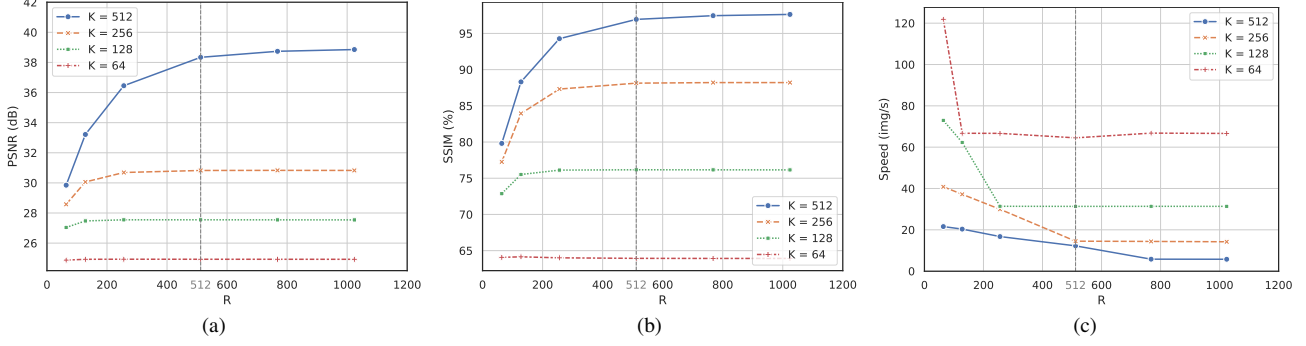


Figure 16. Effect of CP rank (R) on FUTON performance. We vary R while fixing $K \in \{64, 128, 256, 512\}$ for image representation (kodim17 from Kodak dataset). (a) Increasing R improves PSNR, with diminishing returns beyond $R = 512$. (b) SSIM exhibits similar saturation behavior. (c) Inference speed degrades hyperbolically with R due to increased contraction cost (Figure 3). The vertical dashed line at $R = 512$ indicates the baseline configuration used in the main experiments.

varies $R \in \{64, 128, 256, 512, 768, 1024\}$ for fixed $K \in \{64, 128, 256, 512\}$. For each fixed K , reconstruction quality increases with R (Figures 16a and 16b), but improvements saturate beyond $R = 512$ across all K , indicating that natural images admit low-rank spectral structure in the Fourier domain, consistent with classical observations on frequency-domain compressibility.

Figure 16c highlights the associated computational trade-off: inference speed decreases roughly hyperbolically with R , *e.g.*, from over 20 img/s at $R = 64$ to around 12 img/s at $R = 512$ for $K = 512$. This trend matches the $\mathcal{O}(2KR + 5R)$ complexity in Section 4.2 and suggests $R = 512$ as a good operating point on this image, balancing accuracy and throughput.

Number of Basis Functions (K). The number of basis functions K determines the spectral resolution of FUTON’s representation. Figure 17 presents results for $K \in \{64, 128, 256, 512, 768, 1024\}$ with fixed $R \in \{64, 128, 256, 512\}$. Across all ranks, increasing K to $K = 512$ monotonically improves reconstruction quality (Figures 17a and 17b). The improvement is most pronounced at higher ranks: with $R = 512$, PSNR increases from around 25 dB at $K = 64$ to over 37 dB at $K = 512$, a 12 dB gain. In contrast, with $R = 128$, the gain over the same range is only around 8 dB.

This interaction between K and R reflects the joint role of spectral resolution and low-rank capacity. Larger K exposes higher-frequency components, but exploiting these components requires sufficient rank R to represent the corresponding coefficients. Conversely, increasing R without adequate K limits the highest representable frequency, capping reconstruction quality and explaining why the highest performance is achieved in the upper-right region of the

Table 3. Comparison of basis functions (φ) on FUTON. Results averaged over the Kodak dataset for image representation with $R = K = 512$. The best results are **bold**, and the second-best are underlined.

Basis Function (φ)	# Params	PSNR (dB) \uparrow	SSIM (%) \uparrow	Speed (img/s) \uparrow
Chebyshev	526K	33.29	92.80	<u>2.14</u>
Legendre	526K	<u>33.33</u>	<u>92.75</u>	2.12
Cosine	526K	37.12	96.53	12.28

K - R space.

Figure 17c shows that inference speed decreases hyperbolically with K , consistent with FUTON’s favorable computational scaling in K . The per-coordinate evaluation cost depends only linearly on K (Section 4.2), enabling FUTON to leverage high spectral resolution without proportional computational overhead, a key advantage over grid-based representations.

Basis Function ($\varphi(\cdot)$). The choice of one-dimensional orthonormal basis $\varphi(\cdot)$ fundamentally determines FUTON’s spectral representation. We compare three classical orthonormal bases on $L^2([0, 1])$: (1) cosine basis (1), (2) Legendre polynomials, and (3) Chebyshev polynomials of the first kind. All three satisfy the completeness property required by Theorem 1, ensuring universal approximation. However, their computational and representational characteristics differ substantially.

Table 3 presents quantitative results averaged over the Kodak dataset. The cosine basis achieves 37.12 dB PSNR and 96.53% SSIM, significantly outperforming Legendre (33.33 dB, 92.75%) and Chebyshev (33.29 dB, 92.80%) by over 3.5 dB. Inference speed also favors the cosine basis at 12.28 img/s, nearly 6× faster than polynomial bases

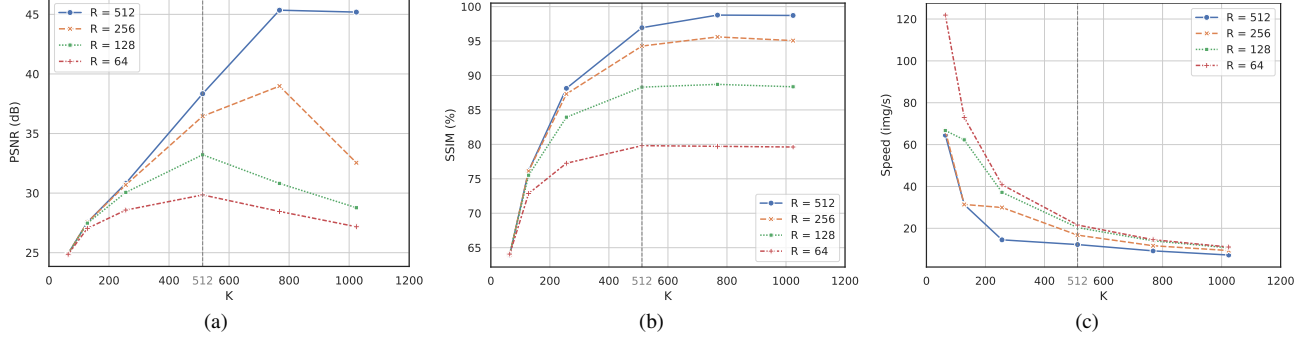


Figure 17. Effect of number of basis functions (K) on FUTON performance. We vary K while fixing $R \in \{64, 128, 256, 512\}$ for image representation (kodim17 from Kodak dataset). (a) Increasing K only up to $K = 512$ improves PSNR, with the highest gains at larger R . (b) Increasing K consistently improves SSIM. (c) Inference speed shows a hyperbolic decline with K , in line with the theoretical time complexity (Figure 3). The vertical dashed line at $K = 512$ indicates the baseline configuration used in the main experiments.

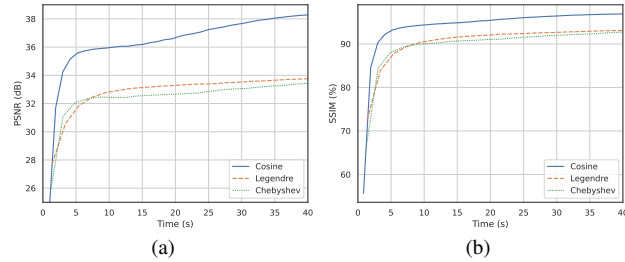


Figure 18. Comparison of basis functions (φ) on FUTON performance. Training curves on image representation (kodim17 from Kodak dataset) for three orthonormal bases: cosine (blue solid line), Legendre (orange dashed line), and Chebyshev (green dotted line). (a) The cosine basis converges significantly faster and achieves higher final PSNR. (b) SSIM exhibits similar trends. Both polynomial bases show comparable but inferior performance, indicating that the spectral properties of the basis significantly impact representational efficiency.

(~ 2 img/s). This performance gap stems from two factors: (1) the cosine basis admits highly efficient evaluation via vectorized trigonometric operations in modern hardware, whereas polynomial bases require recursive computation or explicit polynomial evaluation; and (2) natural images are known to be sparse in the frequency domain, which the cosine basis (closely related to the discrete cosine transform used in JPEG) naturally exploits.

Figure 18 reveals striking differences in convergence behavior. The cosine basis reaches 30 dB within a few seconds, while polynomial bases require over 40 seconds. This rapid convergence likely reflects better conditioning of the optimization landscape when the basis is well-aligned with the signal's intrinsic structure. In contrast, the polynomial bases

exhibit slower, more oscillatory convergence, suggesting less favorable gradient flow through the tensor network.

These findings motivate the use of the cosine basis in all main experiments. While other bases (e.g., wavelets, B-splines) could be explored, the cosine basis provides a favorable balance of universal approximation, computational efficiency, and empirical performance for natural signal representation.